International Journal of Marine Energy 14 (2016) 80–100

Contents lists available at ScienceDirect

International Journal of Marine Energy

journal homepage: www.elsevier.com/locate/ijome

Simulation by discrete mass modeling of offshore wind turbine system with DC link

M. Seixas [a,b,c], R. Melício [a,b,*], V.M.F. Mendes [b,c,*]

[a] IDMEC/LAETA, Instituto Superior Técnico, Universidade de Lisboa, Lisbon, Portugal
[b] Departamento de Física, Escola de Ciências e Tecnologia, Universidade de Évora, Portugal
[c] Department of Electrical Engineering and Automation, Instituto Superior de Engenharia de Lisboa, Lisbon, Portugal

ARTICLE INFO

Article history:
Received 19 December 2014
Revised 3 February 2016
Accepted 18 February 2016
Available online 26 February 2016

Keywords:
Offshore wind turbine system
Discrete mass modeling
DC link
Power converter
Simulation

ABSTRACT

This paper presents an integrated model for an offshore wind turbine taking into consideration a contribution for the marine wave and wind speed with perturbations influences on the power quality of current injected into the electric grid. The paper deals with the simulation of one floating offshore wind turbine equipped with a permanent magnet synchronous generator, and a two-level converter connected to an onshore electric grid. The use of discrete mass modeling is accessed in order to reveal by computing the total harmonic distortion on how the perturbations of the captured energy are attenuated at the electric grid injection point. Two torque actions are considered for the three-mass modeling, the aerodynamic on the flexible part and on the rigid part of the blades. Also, a torque due to the influence of marine waves in deep water is considered. Proportional integral fractional-order control supports the control strategy. A comparison between the drive train models is presented.

* Corresponding authors at: Departamento de Física, Escola de Ciências e Tecnologia, Universidade de Évora, Portugal. Tel.: +351 266 745372; fax: +351 266 745394.
E-mail addresses: ruimelicio@gmail.com (R. Melício), vfmendes@deea.isel.pt (V.M.F. Mendes).

http://dx.doi.org/10.1016/j.ijome.2016.02.002
2214-1669/

Nomenclature

v	perturbed wind speed
v_0	average wind speed
n	kind of the mechanical eigenswing excited by the rotation movement
A_n	magnitude of the eigenswing n
ω_n	eigenfrequency of the n eigenswing
P_b	mechanical power of the wind turbine with dynamic perturbations
P_{bb}	mechanical power captured by the wind turbine without dynamic perturbations
ρ	air density
R	radius of the area cover by the blades, OB part
c_p	power coefficient
ς	pitch angle of the turbine blades
λ_R	tip speed ratio, at radius R
λ_r	local speed ratio, at radius r
r	radius of the rigid part of the blades, OA part
m	order of the harmonic of an eigenswing
a_{nm}	normalized magnitude of g_{nm}
g_{nm}	distribution of the m-order harmonic in the n eigenswing
h_n	modulation of the n eigenswing
φ_{nm}	phase of the m-order harmonic in the n eigenswing
η	wave elevation for x, y position as a function of time
η_a	vector of harmonic wave amplitudes
ϑ	vector of harmonic wave frequencies
ε	vector of harmonic wave phases (random)
ϕ	vector of harmonic wave numbers
ψ	vector of harmonic wave directions
M_{mb}	one and two-mass models, wind turbine mechanical torque
M_{mfb}	three-mass model, wind turbine flexible blade part mechanical torque
M_{mrb}	three-mass model, wind turbine rigid part of the blades mechanical torque
M_{stp}	all models, tower and platform stiffness torque due to floating surface motion
M_{rb}	two-mass model, turbine bearing resistant torque
M_{rah}	two-mass model, hub and blades viscosity airflow resistant torque
M_{sb}	two-mass model, shaft stiffness torsional torque
M_{re}	two and three-mass models, generator bearing resistant torque
M_{rae}	two-mass model, generator viscosity airflow resistant torque
M_e	all models, electric torque
M_{rfb}	three-mass model, flexible blades part bearing resistant torque
M_{sfbh}	three-mass model, shaft stiffness torque between flexible blades part and hub
M_{rh}	three-mass model, hub bearing resistant torque
M_{she}	three-mass model, shaft stiffness torque between hub and generator
ω_w	marine wave frequency
ω_{be}	two-mass model, angular sped between turbine and generator
ω_b	one and two-mass models, angular speed of the turbine
ω_e	all models, angular speed of the generator
ω_{fbh}	three-mass model, angular speed between flexible blades and hub
ω_{fb}	three-mass model, angular speed of the flexible blades
ω_{rbh}	three-mass model, angular speed of the rigid part of the blades plus hub
ω_{he}	three-mass model, angular speed between hub and generator
k_{stp}	all models, stiffness elastic coefficient due to tower and platform in deep water
k_{rb}	two-mass model, turbine bearing friction coefficient
k_{rah}	two-mass model, hub and blades viscosity airflow coefficient
k_{sb}	two-mass model, shaft stiffness elastic coefficient
k_{re}	two and three-mass models, generator bearing friction coefficient

k_{rae}	two-mass model, generator viscosity airflow coefficient
k_{rfb}	three-mass model, blades flexible part bearing friction coefficient
k_{sfbh}	three-mass model, shaft stiffness elastic coefficient between flexible blades and hub
k_{rh}	three-mass model, hub bearing friction coefficient
k_{she}	three-mass model, shaft stiffness elastic coefficient between hub and generator
θ_{be}	two-mass model, angular deviation
θ_b	two-mass model, turbine shaft angular position
θ_e	two and three-mass models, generator shaft angular position
θ_{fbh}	three-mass model, flexible blades angular deviation to the rigid blades plus hub
θ_{fb}	three-mass model, flexible blades shaft angular position
θ_{rbh}	three-mass model, hub shaft angular position
θ_{he}	three-mass model, rigid blades plus hub angular deviation to the generator
J	one-mass model, moment of inertia for blades, hub, tower, platform and generator
J_b	two-mass model, blades, hub, tower and platform moment of inertia
J_e	two and three-mass models, generator moment of inertia
J_{fb}	three-mass model, flexible blades part moment of inertia
J_{rbh}	three-mass model, rigid blades part plus hub, tower and platform moment of inertia
i_{sd}, i_{sq}	stator dq currents
L_{sd}, L_{sq}	stator dq inductances
R_{sd}, R_{sq}	stator dq resistances
u_{sd}, u_{sq}	stator dq voltages
p	number of pairs of poles
L_m	mutual inductance
i_{er}	equivalent rotor current
u_{er}	equivalent rotor voltage
i_{gy}	electric grid injected current
P_e	electric power
R_g	electric grid resistance
L_g	electric grid inductance
u_{gy}	filter voltage
u_y	electric grid voltage
u_{sy}	converter voltage
i_y	converter current
u^*_{dc}	reference voltage
u_{dc1}	capacity bank C_1 voltage, i.e., continuous rectifier output voltage
u_{dc2}	capacity bank C_2 voltage, i.e., inverter input voltage
R_{dc}	submarine cable resistance
L_{dc}	submarine cable inductance
C_{dc}	submarine cable capacity
i_{dc}	submarine cable current

1. Introduction

The global energy demand in 2040 is expected to be about 30% higher than that of 2010 [1], so is predictable that more challenges such as increased environmental problems, depletion of fossil fuels and unstable oil prices will intensify [2]. The majority of the energy used by the society comes from the use of conventional fossil fuels [3], but the use of fossil fuels, accounts for 80% of anthropogenic gas emission [4]. The use of renewable energy sources is crucial in order to decarbonize the energy industry [5] and in recent years there has been a rapid increase in power capacity and energy conversion from these sources. Mostly, in what regards the use of wind energy [6,7]. Although, onshore wind energy conversion is less expensive than offshore, for instance, the costs of operation and maintenance for offshore wind energy conversion are approximately 2–4 times to that of the onshore [8], finding new suitable available onshore sites is becoming difficult, particularly in Europe [9]. Particularly,

developments in offshore wind power were achieved with the research and exploitation on floating wind turbines [10], taking advantage of vast areas of available sea and of favorable wind conditions which are reported as tending to be considerably better and less variable than onshore ones [11].

Offshore structures are influenced by marine wind and wave dynamics. For instance, the authors in [12] consider the influence of the floating support structure motion on the strength of the blades and shaft, and the force induced by the combined rotational, translational and angular motion of the blades due to the coupling effects of the dynamics. Hence, there is a need to access how important are the loads in disturbing the conversion in what regards electric energy quality.

Offshore deployment for conversion of wind energy allows the use of higher rotor dimension due to less restrictions of scale which enables the use of larger turbines. This fact leads to a need for a proper design of the drive train of the wind turbine besides higher requirement of turbine reliability [13]. So, the model for an offshore wind turbine system (OWTS) has to take into account the flexibility of the mechanical structure, due to the height and the tendency to oscillate [14] and will be highly nonlinear. Oversimplification on the modeling of the OWTS could introduce significant error in the value of the results.

As wind energy is increasingly integrated into power systems, electric energy quality is becoming a concern of utmost importance [15]. One of the indices that measure the electric energy quality is the total harmonic distortion (THD). The standard IEEE-519 imposes a maximum limit of 5% for the electrical current THD. While the application of the standard IEEE-519 is not mandatory for OWTS this THD value is followed as a guideline for evaluation purpose.

Variable speed operation technology based on the use of permanent magnet synchronous generator (PMSG) as an alternative to conventional synchronous generators as the advantages generally stated for wind power applications: the higher efficiency, due to null copper losses in the rotor [16]; the exclusion of the gearbox, due to ability to operate at low speed [17]. A variable speed wind turbine equipped with a PMSG needs an electronic full-power converter in order to convert the energy captured from the wind into electric energy at a non-constant frequency into constant one [18]. The type of power transmission technology in offshore depends on the distance between the floating platforms and the grid connection point. For shorter distances, below 50 km, alternated current (AC) can be used, but for longer distances direct current (DC) becomes the most suitable solution, since reduced energy losses are presented [19].

This paper presents a model for the simulation of an OWTS. The model considers an offshore variable-speed turbine with a power output of 2 MW in deep water equipped with a permanent magnet synchronous generator using full-power two-level converter (TLC). Also, a submarine cable is considered to guide electrical energy through a DC link from the variable frequency source to the injected energy into the electric grid with constant frequency. The wind turbine part of the system rests on a tri-column triangular floating platform partially submerged with the wind turbine located on top of one of the columns, and the other two columns have more ballast to stabilize the entire platform. The platform is moored using a conventional catenary mooring system [20] linking the floating platform to structures made of concrete, which are in turn anchored to the marine soil. The mooring system is needed for the floating platform in order to hold the device in place [21]. The layout of the OWTS is shown in Fig. 1.

The mechanical drive train, the structure and the moving floating surface dynamics is considered by three approaches, respectively, one-mass, two-mass or three-mass in order to discuss which are more appropriated in detaining the THD. The three-mass model is considered in order to isolate the aerodynamics influence on the flexible part of the blades from the rigid one. This isolation is associated with the two mechanical torques acting on the respective parts of the blades. The controllers used in the converters are proportional integral (PI) ones. Also, pulse width modulation (PWM) by space vector modulation (SVM) associated with sliding mode (SM) is used for controlling the converters.

The rest of the paper is organized as followed: Section 2 presents the mechanical modeling, taking into consideration the dynamics associated with the action excited by wind on all physical structure on a two-mass modeling for the rotor of the wind turbine and generator. Section 3 presents the electric modeling, taking into consideration the TLC, the submarine cable and the electric grid. Section 4 presents the fractional calculus theory. Section 5 presents the control modeling: PWM by SVM associated with SM for controlling the converter. Section 6 presents the case studies and the simulation results, using Matlab/Simulink language. Section 7 presents concluding remarks.

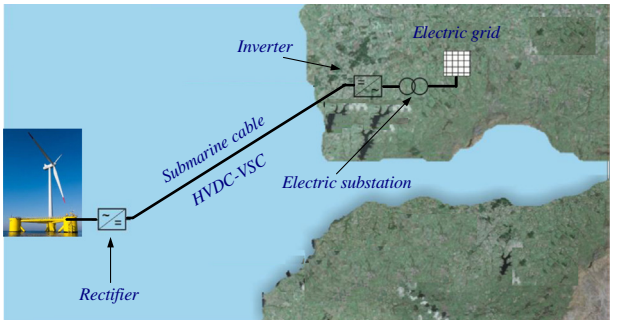

Fig. 1. Layout of the offshore wind energy conversion system.

2. Mechanical modeling

The wind speed has a model consisting in a finite sum of harmonic terms with frequencies range in 0.1–10 Hz, given by:

$$v = v_0\left[1 + \sum_n A_n \sin(\omega_n t)\right] \tag{1}$$

The mechanical power of the wind turbine has a model taking into consideration three perturbations of the dynamics associated with the action excited by the wind on all physical structure [22]. The mechanical power is given by:

$$P_b = P_{bb}\left[1 + \sum_{n=1}^{3} I_n(t)\right] \tag{2}$$

where

$$P_{bb} = \frac{1}{2}\rho\pi R^2 v^3 c_p \tag{3}$$

The power coefficient is a function of the tip speed ratio and of the pitch angle. The determination of this coefficient requires the use of blade element theory and the knowledge of blade geometry. Normally, numerical approximations are advised as for instance the one developed in [23] followed in this paper and given by:

$$c_p = 0.73\left(\frac{151}{\lambda_i} - 0.58\varsigma - 0.002\varsigma^{2.14} - 13.2\right)e^{-\frac{18.4}{\lambda_i}} \tag{4}$$

where

$$\lambda_i = \frac{1}{\frac{1}{(\lambda - 0.02\varsigma)} - \frac{0.003}{(\varsigma^3+1)}} \tag{5}$$

The mechanical power in (2) is computed by a multiplicative term (3) given by the well-known formula for the mechanical power captured by the wind turbine without dynamic perturbations [22]. The perturbations considered are three, respectively: I_1 the asymmetry in the turbine, I_2 the vortex tower interaction and I_3 the eigenswings in the blades. Both perturbations are modeled by a sum given by:

$$I_n(t) = A_n\left(\sum_{m=1}^{2} a_{nm} g_{nm}(t)\right) h_n(t) \tag{6}$$

where

$$g_{nm}(t) = \sin\left(\int_0^t m\omega_n(t')dt' + \varphi_{nm}\right) \tag{7}$$

The dynamics associated with the asymmetry in the turbine is assessed considering the following data: $A_1 = 0.01$, $a_{11} = 4/5$, $a_{12} = 1/5$, $\omega_1(t) = \omega_t(t)$, $\varphi_{11} = 0$, $\varphi_{12} = \pi/2$.

The dynamics associated with the vortex tower interaction is assessed considering the following data: $A_2 = 0.08$, $a_{21} = 1/2$, $a_{22} = 1/2$, $\omega_2(t) = 3\omega_t(t)$ $\varphi_{21} = 0$, $\varphi_{22} = \pi/2$.

The dynamics associated with the eigenswings in the blades is assessed considering the following data: $A_3 = 0.15$, $a_{31} = 1$, $\omega_2(t) = 1/2[g_{11}(t) + g_{21}(t)]$, $\varphi_{31} = 0$.

The marine wave model [24] for all the drive train models is given by:

$$\eta(x,y,t) = \sum_{i=1}^{n} \eta_a(i)\cos\left[\vartheta(i)t + \varepsilon(i) - \phi(i)(x\cos(\psi(i)) + y\sin(\psi(i))\right] \tag{8}$$

The elastic behavior of the tower and platform due to the influence of marine waves, in deep water, for all the drive train models causes a resistant torque [25] given by:

$$M_{stp} = k_{stp}\ \omega_w \tag{9}$$

The behavior of the mechanical drive train of an OWTS has a model consisting in a set of discrete inertia masses connected together by springs and dampers. The one-mass drive train model considers all inertia components lumped together, i.e., modeled as a single rotating mass as shown in Fig. 2.

The mechanical torque of the wind turbine subject to a wind without perturbations, in the case of the drive train described by a shaft with one or two-mass model, considering (3), is given by:

$$M_{mb} = \frac{1}{2}\frac{\rho\pi R^5\omega_b^2}{\lambda_R^3}c_p \tag{10}$$

The equation for the one-mass model is based on the second law of Newton, deriving the state equation for the rotor angular speed at the wind turbine, given by:

$$\frac{d\omega_b}{dt} = \frac{1}{J}\left(M_{mb} + M_{stp} - M_e\right) \tag{11}$$

The drive train configured by two-mass model has a first mass to concentrate inertia of the blades, hub, tower and platform; a second mass to concentrate the generator inertia. This configuration is shown in Fig. 3.

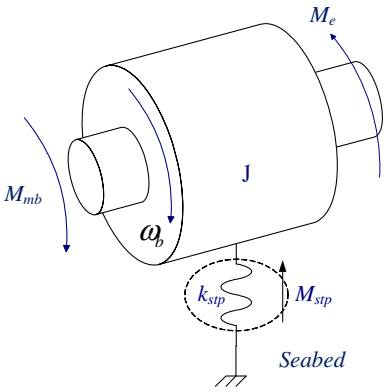

Fig. 2. One-mass drive train model.

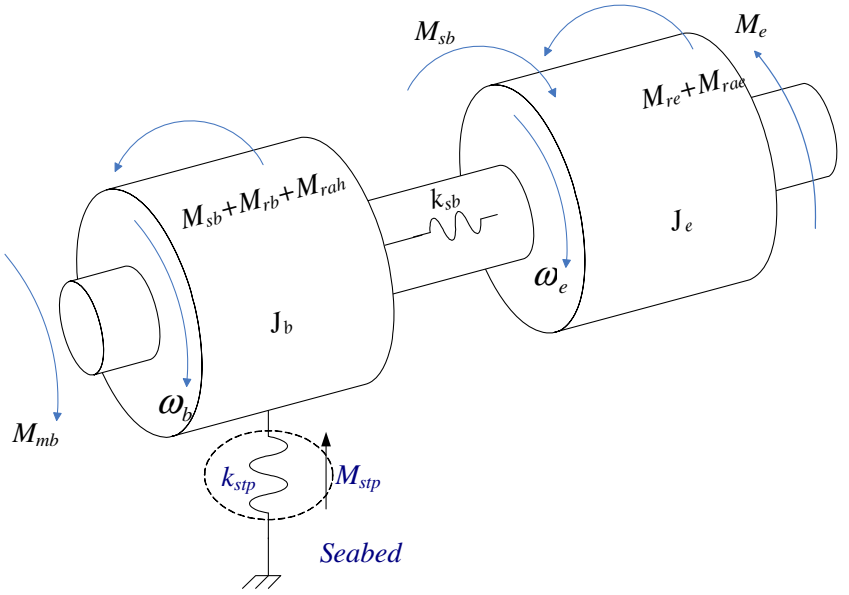

Fig. 3. Two-mass drive train model.

On the two-mass model the angular deviation due to the stiffness coefficient between turbine and generator is given by:

$$\theta_{be} = \theta_b - \theta_e \tag{12}$$

So, the angular speed of the stiffness element between turbine and generator is given by:

$$\omega_{be} = \omega_b - \omega_e \tag{13}$$

The resistant torque due to friction on the turbine bearing is given by:

$$M_{rb} = k_{rb}\omega_b \tag{14}$$

The resistant torque due to viscosity with the air flow on the rotor hub and the blades is given by:

$$M_{rah} = k_{rah}\omega_b^2 \tag{15}$$

The stiffness torsional torque due to the elastic behavior of the shaft is given by:

$$M_{sb} = k_{sb}\theta_{be} \tag{16}$$

The resistant torque due to friction on the generator bearing is given by:

$$M_{re} = k_{re}\omega_e \tag{17}$$

The resistant torque due to viscosity with the air flow on the generator is given by:

$$M_{rae} = k_{rae}\omega_e^2 \tag{18}$$

The equations for the two-mass model are based on the torsional version of the second law of Newton, deriving the state equation for the rotor angular speed at the wind turbine and for the rotor angular speed at the generator, given by:

$$\frac{d\omega_b}{dt} = \frac{1}{J_b}\left(M_{mb} + M_{stp} - M_{rb} - M_{rah} - M_{sb}\right) \tag{19}$$

$$\frac{d\omega_e}{dt} = \frac{1}{J_e}(M_{sb} - M_{re} - M_{rae} - M_e) \tag{20}$$

The increase in size of the wind turbines implies that the blades are more flexible and tend to bend. Since the blade bending occurs at a significant distance from the joint between the blades and the hub is admissible to model the blades by splitting them in two parts. The blade bending dynamics is explained by a torsional system as shown in Fig. 4.

The first part, OA is defined from the root of the blade to a point of radius r of his wingspan with a rigid behavior; the second part AB is defined from the point of radius r to the edge of the blade with a flexible behavior. The rigid part of the blades is formed by sectors OA1, OA2 and OA3and the flexible part of the blades is formed by sectors A1B1, A2B2 and A3B3.

One of the aeroelastic problems for large wind turbines is due to the fact that the lead-lag and flap frequencies of the blades may come closer together during the up-scaling of the turbines. This, in combination with stalled flow can result in aeroelastic instabilities [26]. The damage resulted from severe aeroelastic instabilities producing longitudinal cracks on the flexible part of the blade near the root. The lead-lag and flap aeroelastic stability of wind turbine blade sections is simulate as a model resulting from the combination of a spring–mass–damper–equivalent structural model [27]. The drive train configured by three masses has a first mass to concentrate the inertia of the flexible part of the blades; a second mass to concentrate the rigid part of the blades, hub, tower and platform; a third mass to concentrate the inertia of the generator similar to the second mass of the two-mass model. The connection between the three masses is made through elastic couplings [28]. The three-mass model is shown in Fig. 5.

Assume a radius r of 2.5 m for the rigid part of the blades, as shown in Fig. 6.

The modeling analysis uses the following assumptions: (1) the wind speed is the same across the blade radius; (2) the blade span has a modeling consisting of two different rigid blades associated with the two blade parts; (3) the blade angular speed in flexible and rigid part is almost the same and have very small fluctuations over the average angular speed; (4) the power coefficient for both parts as a function of the respective speed ratios has the same value.

The tip speed ratio λ_R, defined as the ratio of the blade tip speed to the wind speed is given by:

$$\lambda_R = \frac{\omega_{fb} R}{v} \tag{21}$$

The local speed ratio λ_r, define as the ratio of the rotor speed at some intermediate radius to the wind speed [29] is given by:

$$\lambda_r = \frac{\omega_{rbh} r}{v} \tag{22}$$

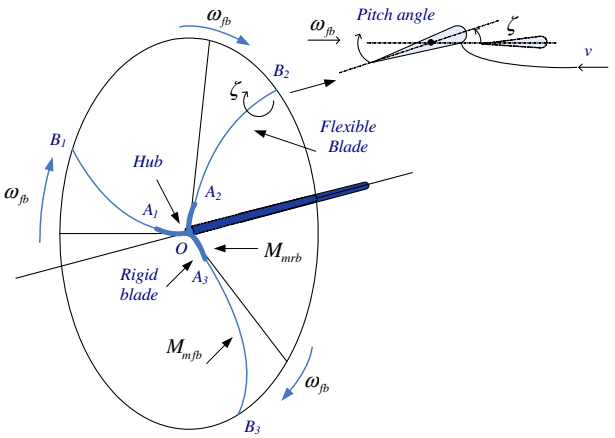

Fig. 4. Blade bending dynamic system.

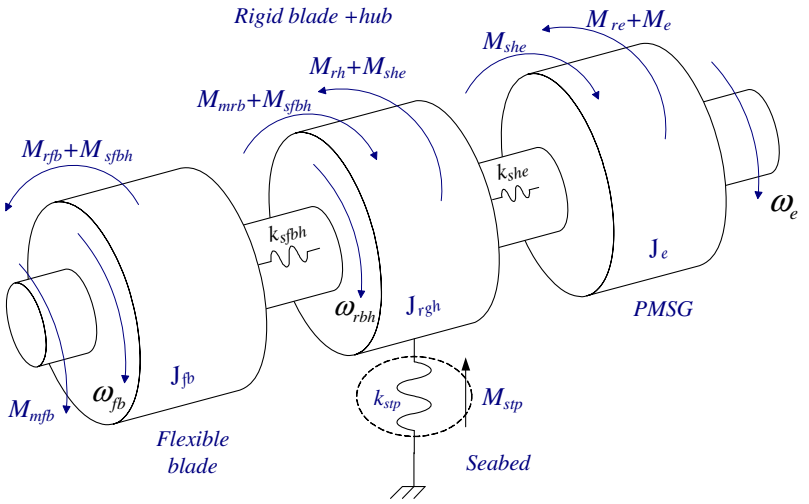

Fig. 5. Three-mass drive train model.

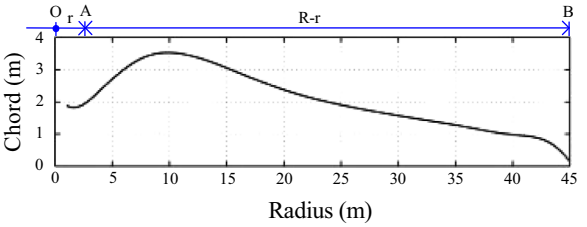

Fig. 6. Blade radius r and R.

The relation between the respective speed ratios, taking into account the assumptions, is given by:

$$\frac{\lambda_r}{\lambda_R} = \frac{r}{R} \quad \text{with} \quad \omega_{fb} \cong \omega_{rbh} \tag{23}$$

The mechanical power for the blade flexible part is given by:

$$P_{fb} = \frac{1}{2}\rho\pi(R^2 - r^2)v^3 c_p \tag{24}$$

The mechanical power for the rigid part of the blades is given by:

$$P_{rb} = \frac{1}{2}\rho\pi r^2 v^3 c_p \tag{25}$$

The mechanical torque of the flexible part of the blades subject to a wind without perturbations, in the case of the drive train described by a shaft with three masses, considering (21) and (24), is given by:

$$M_{mfb} = \frac{1}{2}\frac{\rho\pi\left(R^2 - r^2\right)\omega_{fb}^2 R^3}{\lambda_R^3} c_p \tag{26}$$

The mechanical torque of the rigid part of the blades subject to a wind without perturbations, in the case of the drive train described by a shaft with three masses, considering (22) and (25), is given by:

$$M_{mrb} = \frac{1}{2}\frac{\rho\pi r^5 \omega_{rbh}^2}{\lambda_r^3} c_p \tag{27}$$

On the three-mass model the angular deviation due to the stiffness coefficient between flexible blades part and hub is given by:

$$\theta_{fbh} = \theta_{fb} - \theta_{rbh} \tag{28}$$

So, the angular speed of the stiffness element between flexible blade part and hub has to satisfy a relation given by:

$$\omega_{fbh} = \omega_{fb} - \omega_{rbh} \tag{29}$$

The angular deviation due to the stiffness coefficient between hub and generator is given by:

$$\theta_{he} = \theta_{rbh} - \theta_e \tag{30}$$

So, the angular speed of the stiffness element between hub and generator is given by:

$$\omega_{he} = \omega_{rbh} - \omega_e \tag{31}$$

The resistant torque due to friction on the flexible blade part bearing is given by:

$$M_{rfb} = k_{rfb}\omega_b \tag{32}$$

The stiffness torsional torque due to the elastic behavior of the shaft between the flexible blade part and the hub is given by:

$$M_{sfbh} = k_{sfbh}\theta_{fbh} \tag{33}$$

The resistant torque due to friction on the hub bearing is given by:

$$M_{rh} = k_{rh}\omega_{rbh} \tag{34}$$

The stiffness torsional torque due to the elastic behavior of the shaft between the hub and the generator is given by:

$$M_{she} = k_{she}\theta_{he} \tag{35}$$

The equations for the three-mass model are based on the torsional version of the second law of Newton, deriving the state equations for the rotor angular speed at the flexible blade part, the rotor angular speed at the rigid part of the blades plus hub of the wind turbine and for the rotor angular speed at the generator, given by:

$$\frac{d\omega_{fb}}{dt} = \frac{1}{J_{fb}}\left(M_{mfb} - M_{rfb} - M_{sfbh}\right) \tag{36}$$

$$\frac{d\omega_h}{dt} = \frac{1}{J_{rbh}}\left(M_{sfbh} + M_{mrb} + M_{stp} - M_{rh} - M_{she}\right) \tag{37}$$

$$\frac{d\omega_e}{dt} = \frac{1}{J_e}\left(M_{she} - M_{re} - M_e\right) \tag{38}$$

3. Electric modeling

The equations for modeling a PMSG are shown in [30] and are given by:

$$\frac{di_{sd}}{dt} = \frac{1}{L_{sd}}\left(u_{sd} + p\omega_e L_{sq} i_{sq} - R_{sd} i_{sd}\right) \tag{39}$$

$$\frac{di_{sq}}{dt} = \frac{1}{L_{sq}}\left[u_{sq} - p\omega_e\left(L_{sd} i_{sd} + L_m i_{er}\right) - R_{sq} i_{sq}\right] \tag{40}$$

with the electric power given by:

$$P_e = [\, u_{sd} \quad u_{sq} \quad u_{er} \,][\, i_{sd} \quad i_{sq} \quad i_{er} \,]^T \tag{41}$$

But in (41) due to the consideration of avowing demagnetization of the permanent magnet in the PMSG [31], a null reference stator direct component current $i_{sd}^* = 0$ has to be imposed.

The AC–DC–AC TLC is implemented with twelve unidirectional commanded insulated gate bipolar transistors in order to implement the rectifier and the inverter functionality [15]. The configuration considered in this paper for the OWTS with TLC is shown in Fig. 7.

The TLC is an AC–DC–AC converter, having six transistors identified by S_{ik}, used as a rectifier and with six similar transistors used as an inverter. The rectifier is connected between the PMSG and a capacitor bank. The inverter is connected between this capacitor bank and a second order filter, which in turn is connected to an electric grid. The grouping of two transistors connected to the same phase constitutes the arm y of the converter. The switching variable γ_y is used to identify the state of the transistor h in the leg y of the TLC ascertain the switching function of each transistor. The index h with $h \in \{a, b\}$ recognize the transistor. The index y with $y \in \{a, b, c\}$ recognizes the arms for the rectifier and $y \in \{d, e, f\}$ recognizes the arms for the inverter. The valid constrains [32,33] for the γ_y of each arm y are given by:

$$\gamma_y = \begin{cases} 1, & (S_{ay} = 1 \quad \text{and} \quad S_{by} = 0) \\ 0, & (S_{by} = 1 \quad \text{and} \quad S_{ay} = 0) \end{cases} \quad y \in \{a, \ldots, f\} \tag{42}$$

The rectifier input voltage is given by:

$$u_{sy} = \frac{1}{3}\left(2\gamma_y - \sum_{\substack{j=a \\ j\neq y}}^{c} \gamma_j\right) u_{dc1}, \quad y \in \{a, b, c\} \tag{43}$$

The state equation of the DC voltage at the capacity bank C_1 terminals is given by:

$$\frac{du_{dc1}}{dt} = \frac{1}{C_1 + C_{dc}}\left(\sum_{y=a}^{c} \gamma_y i_y - i_{dc}\right) \tag{44}$$

The impedance of the submarine cable is represented by a π equivalent electric circuit model, for the medium line modeling is used [24]. The current in the submarine cable is given by:

$$\frac{di_{dc}}{dt} = \frac{1}{L_{dc}}(u_{dc1} - u_{dc2} - R_{dc} i_{dc}) \tag{45}$$

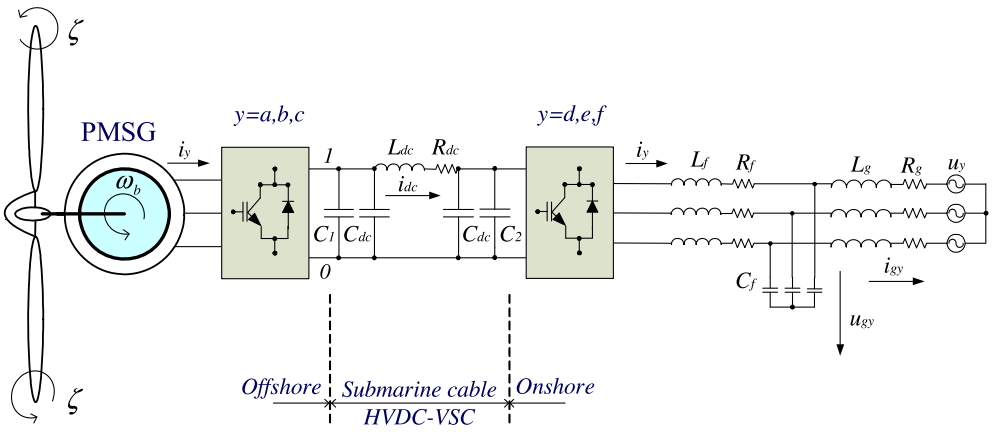

Fig. 7. OWTS with TLC and submarine cable.

The state equation of the DC voltage at the capacity bank C_2 terminals is given by:

$$\frac{du_{dc2}}{dt} = \frac{1}{C_2 + C_{dc}} \left(i_{dc} - \sum_{y=d}^{f} \gamma_y i_y \right) \tag{46}$$

The inverter output voltage is given by:

$$u_{sy} = \frac{1}{3} \left(2\gamma_y - \sum_{\substack{j=d \\ j \neq y}}^{f} \gamma_j \right) u_{dc2}, \quad y \in \{d, e, f\} \tag{47}$$

The electric grid has a model consisting in an equivalent three-phase active symmetrical circuit with a series of a resistance and an inductance. Hence, for electric current injected into the electric grid, see Fig. 7 the state equation is given by:

$$\frac{di_{gy}}{dt} = \frac{1}{L_g} (u_{gy} - R_g i_{gy} - u_y), \quad y \in \{d, e, f\} \tag{48}$$

4. Fractional calculus

Fractional-order controller strategy is supported by the theory of fractional calculus. Fractional calculus generalizes ordinary differentiation and integration calculus and it can be seen as the extension of it to include an arbitrary, non-integer order, including a complex order. Applications of fractional calculus theory in controller field have been proposed for OWTS [15] in order to achieve a less harmonic content. The use of fractional-order PI^{μ} controllers can improve properties and controlling abilities over classical PI controllers [34].

The fractional-order operator denoted by ${}_aD_t^{\mu}$ [35] is given by:

$${}_aD_t^{\mu} = \begin{cases} \frac{d^{\mu}}{dt^{\mu}}, & \Re(\mu) > 0 \\ 1, & \Re(\mu) = 0 \\ \int_a^t (d\tau)^{-\mu}, & \Re(\mu) < 0 \end{cases} \tag{49}$$

where $\Re(\mu)$ is the real part of the μ, if $\Re(\mu) > 0$ then μ is the order of the derivative, if $\Re(\mu) < 0$ then $-\mu$ is the order of the integration.

Several approaches are possible for defining a fractional-order derivative and a fractional-order integral. The Riemann–Liouville definition is the most frequently encountered one. The Caputo definition for the fractional-order derivative is given by:

$${}_a^{C}D_t^{\mu} f(t) = \frac{1}{\Gamma(n-\mu)} \int_a^t \frac{f^{(n)}(\tau)}{(t-\tau)^{\mu-n+1}} d\tau \tag{50}$$

where:

$$\Gamma(x) \equiv \int_0^{\infty} y^{x-1} e^{-y} dy \tag{51}$$

while the Riemann–Liouville definition of fractional-order integral is given by:

$${}_aD_t^{-\mu} f(t) = \frac{1}{\Gamma(\mu)} \int_a^t (t-\tau)^{\mu-1} f(\tau) d\tau \tag{52}$$

$\Gamma(x)$ is the Euler's Gamma function, a and t are the limits of the integration, and μ identifies the fractional order.

In this paper, μ is assumed as a real number that satisfies the restrictions $0 < \mu < 1$. Also, $a = 0$ and the following notational convention ${}_0D_t^{-\mu} \equiv D_t^{-\mu}$ are assumed.

Other used approach is Grünwald–Letnikov definition: for the fractional-order derivative given by:

$$ {}_aD_t^{\mu} f(t) = \lim_{\substack{h \to 0 \\ nh \approx t-a}} h^{-\mu} \sum_{r=0}^{n} (-1)^{\mu} f(t - rh) \tag{53} $$

for the fractional-order integral given by:

$$ {}_aD_t^{-\mu} f(t) = \lim_{h \to 0} h^{\mu} \sum_{r=0}^{\frac{t-a}{h}} \frac{\Gamma(\mu + r)}{r!\Gamma(\mu)} f(t - rh) \tag{54} $$

The fractional-order controller design is characterized in comparison with the classic one by having the additional advantage of augmenting the freedom for achieving an enhanced behavior [34], due to the advantage of having more criterion than the classical one, implied by the ability of weighting the past effects at each action of the controller. A fractional-order controller has a dynamical behavior described by a fractional differential integral equation with a derivative or an integral having at least a non integer order.

5. Control modeling

A fractional-order PI^{μ} controller implement the controller strategy considered in the simulation for the variable-speed operation of the wind turbine with PMSG and a TLC. The fractional-order PI^{μ} controller differential equation is given by:

$$ f(t) = K_p e(t) + K_i D_t^{-\mu} e(t) \tag{55} $$

The fractional-order PI^{μ} has the advantage of being more flexible than the classical PI controller. This advantage is due to the existence of one more adjustable parameter, accounting for the intensity of integration. The transfer function of the fractional-order controller, using the Laplace transform on (55), is given by:

$$ G(s) = K_p + K_i s^{-\mu} \tag{56} $$

Taking the order of integration μ equal to one in (56), a classical PI controller is obtained. The option [36] is followed for assessing the values of the parameters and circumvents the modeling of a mathematical programming problem, which is a different modeling. This type of option is the one normal in electric power systems to avoid a cumbersome modeling [37] for a fine tuning of parameters. The values of the parameters are given by a tradeoff compromised involving robustness and dynamics performance using tuning rules and favoring the range [0.4, 0.6] for the order of integration μ.

The design of PI^{μ} controller follows the tuning rules in [36]. Power converters are modeled as a pure delay [15] and the left-over dynamics are modeled with a second order equivalent transfer function, following the identification of a step response. The control strategy of the OWTS with a TLC using PI^{μ} controllers has the block diagram is shown in Fig. 8.

The convenient vector selection to ensure stability for the TLC, after being processed by the hysteresis comparator in the block of SM control and SVM are given in [15]. The SM control is a lower level of control as is normally implemented with the PI^{μ} controller, for triggering the converters transistors is used pulse width modulation (PWM) by SVM supplemented with SM. Physical constraints due to the power semiconductors have to be considered during design phase and simulation studies. Particularly, the constraint of power semiconductors due to the fact of having a non-infinite switching frequency, implying that an error on the electric current between the reference value and the control value have to be tolerated. For instances, finite value of switching frequency of 2 kHz, 5 kHz or 10 kHz are normally reported.

Based on the Concordia $(\alpha - \beta)$ transformation, in order to guarantee that the system follows the sliding surface $A(e_{\alpha\beta}, t)$, where $e_{\alpha\beta}$ is the error on the electric currents in the $\alpha\beta$-plane [32], is necessary that the error trajectory in the neighboring of the sliding surface observes the stability conditions given by:

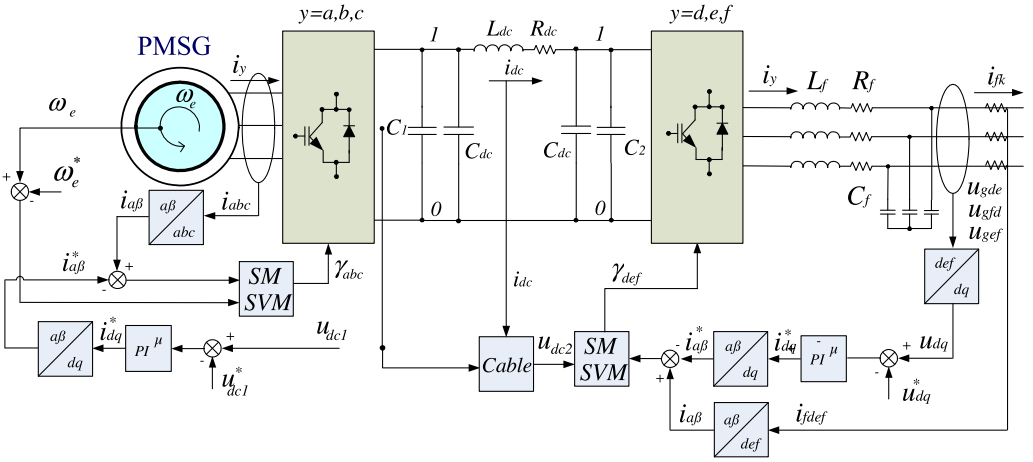

Fig. 8. Diagram of an OWTS with TLC employing PI^{μ} controllers.

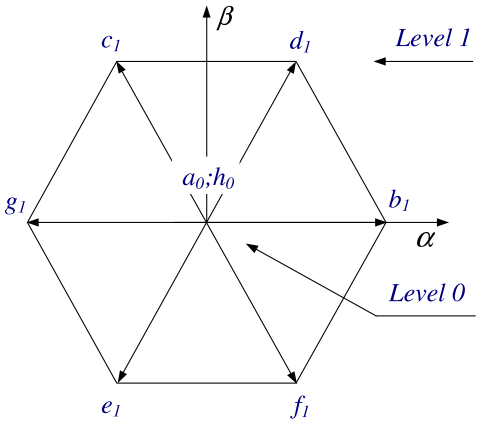

Fig. 9. Output voltage vectors for the TLC.

$$A(e_{\alpha\beta},t)\frac{dA(e_{\alpha\beta},t)}{dt}<0 \tag{57}$$

The sliding surface in current practice is chosen in way to allow a small error $\tau>0$ for $A(e_{\alpha\beta},t)$. This is due to power semiconductors switching finite frequency. But, for the simulation studies, an implementation of the switching strategy considered may be implemented by hysteresis comparators performing accordingly to the condition given by:

$$-\tau<A(e_{\alpha\beta},t)<+\tau \tag{58}$$

This implementation of the switching strategy is implemented in the SM, SVM block, see Fig. 7. The outputs of the hysteresis comparators are the integer variables $\delta_{\alpha\beta}=(\delta_\alpha,\delta_\beta)$ [32]. For the TLC the output voltage vectors lie between level 0 and level 1, vector a_0 and h_0 are vectors for level 0 and vectors from b_1 trough g_1 are vectors for level 1. The output voltage vectors in the $\alpha\beta$ plane are shown in Fig. 9.

The integer voltage variables δ_α and δ_β are given by:

$$\delta_\alpha,\delta_\beta\in\{-1,0,1\} \tag{59}$$

For the TLC, the generic output voltage vector selection [32,33] is shown in Table 1.

Table 1
Generic output voltage vectors selection for the TLC, with the redundant inner vectors.

$\delta_\beta \setminus \delta_\alpha$	-1	0	1
-1	e_1	$e_1; f_1$	f_1
0	g_1	$a_0; h_0$	b_1
1	c_1	$c_1; d_1$	d_1

6. Case study

The wind speed for the operational range of the OWTS is from 5 m/s to 20 m/s and the switching frequency for transistors are 10 kHz. The mechanical eigenswings are given in [22]. The significant wave height and the frequency are respectively 10 m and 0.25 Hz. A rated electric power of 2 MW is considered for the OWTS, more data is in Table 2.

The dynamics associated with the action excited by the wind on all physical structure is considered by a wind speed profile without perturbations (blue) or with perturbations (green) as shown in Fig. 10.

The marine elevation is shown in Fig. 11.

The fractional controllers parameters are $\mu = 0.5$, $K_p = 50$ and $K_i = 2.6$ following [36]. The Discrete Fourier Transform is used to compute the total harmonic distortion THD given by:

$$\text{THD } (\%) = 100\frac{\sqrt{\sum_{H=2}^{50} X_H^2}}{X_F} \tag{60}$$

Table 2
OWTS data.

Turbine moment of inertia	5500×10^3 kg m^2
Turbine rotor diameter	90 m
Hub height	80 m
Tip speed	17.64–81.04 m/s
Rotor speed	6.9–31.6 rpm
Generator rated power	2000 kW
Generator moment of inertia	400×10^3 kg m^2

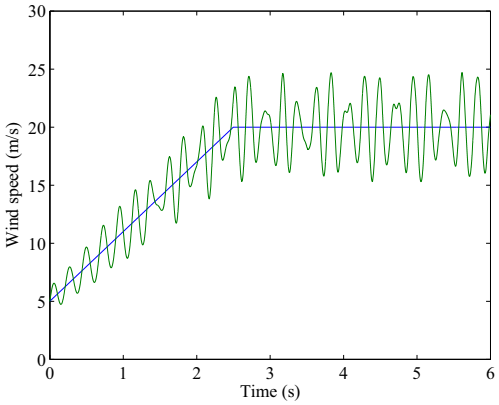

Fig. 10. Wind speed without perturbations (blue) or with perturbations (green).

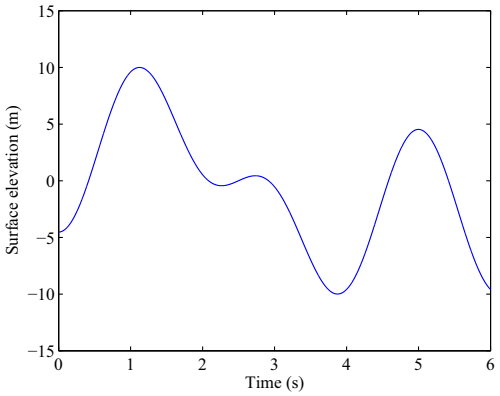

Fig. 11. The marine elevation.

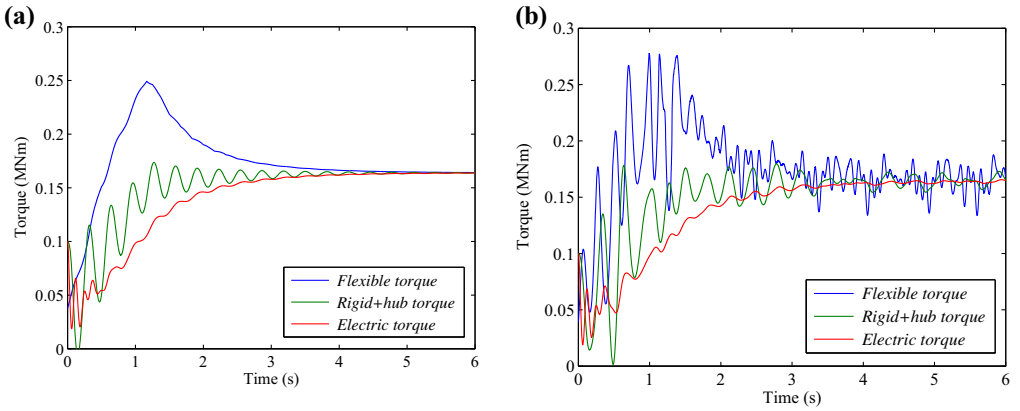

Fig. 12. Three-mass model: flexible blade torque, rigid blade plus hub torque, and electric torque. (a) Wind without perturbations; (b) wind with perturbations.

where X_H is the root mean square (RMS) value of the harmonic H, X_F is the RMS value of the fundamental component.

The flexible blade torque (blue), the rigid part of the blades plus hub torque (green) and the electric torque (red) for the three-mass model of the OWTS, without and with wind perturbations are shown Fig. 12.

For a wind without perturbations the flexible blade torque, the rigid part of the blades plus hub torque and the electric torque show a difference due to the kinetic energy to be stored in the respective masses, but after that both torques converge to almost the same value, i.e., the dynamics enters on an almost stationary state. For a wind with perturbations the flexible blade torque is significantly perturbed by the wind, presenting an oscillatory behavior due to the perturbations associated with the energy captured, which is a significant portion due to the relative lengths of the flexible blade part in comparison with the rigid one. The rigid part of the blades plus hub torque is also affected but with smaller intensity. The electric torque is almost the same as with a case of wind without perturbations, i.e., an identical behavior towards the stationary state is observed.

The rotor angular speed of the flexible blade (blue), the rotor angular speed of the rigid part of the blades plus hub (green) and the rotor angular speed of the generator (red), without and with wind perturbations are shown in Fig. 13.

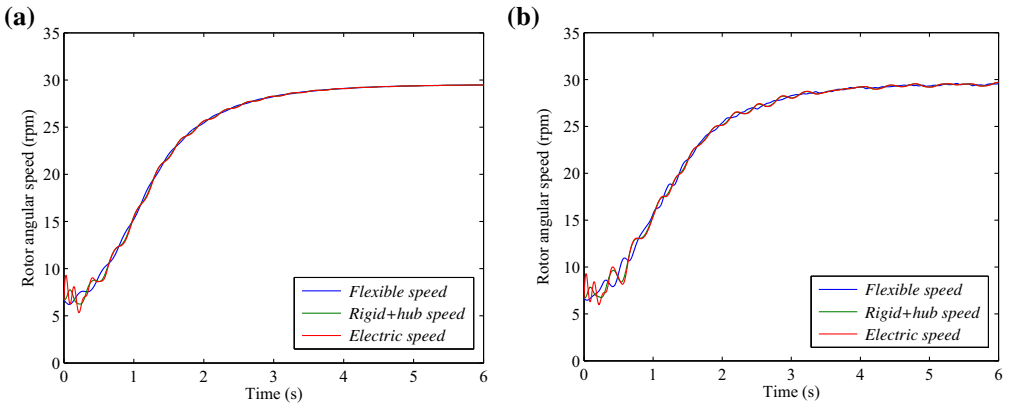

Fig. 13. Three-mass model: rotor angular speed of the flexible blade, rigid blade plus hub and generator. (a) Wind without perturbations; (b) wind with perturbations.

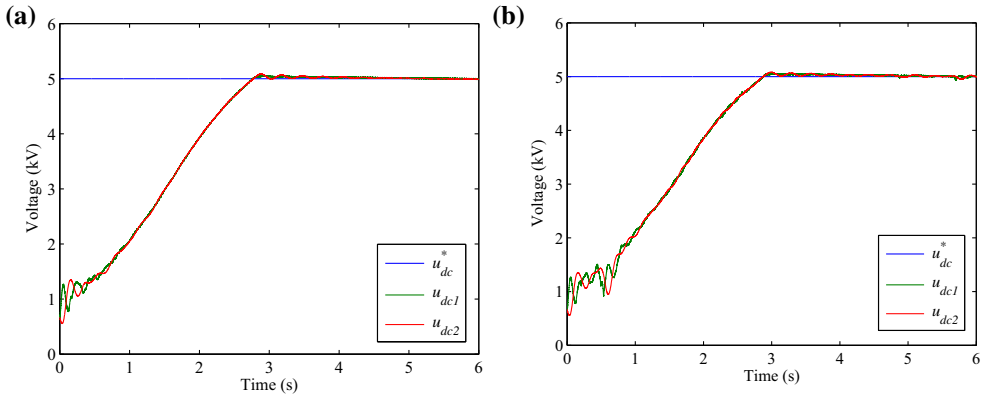

Fig. 14. Three-mass model: reference voltage, continuous rectifier output and inverter input voltages for the submarine cable. (a) Wind without perturbations; (b) wind with perturbations.

For a wind without perturbations the rotor angular speed of the flexible blade, the rotor angular speed of the rigid part of the blades plus hub and the rotor angular speed of the generator show that the mass speeds have a convergence to a value identifying the stationary state. For a wind with perturbations the rotor angular speeds have a convergence to a value identifying the stationary state with added small oscillations in comparison with the wind without perturbations.

The submarine cable results for the reference voltage (blue) in what regard the continuous rectifier output (green) and the inverter input (red) voltages, without and with wind perturbations are shown Fig. 14.

For a wind without perturbations Fig. 14a shows that the reference voltage on the capacitor banks is attained with a satisfactory convergence in a few seconds. For a wind with perturbations Fig. 14b shows that the wind perturbations are attenuated and almost after a few seconds cease to have influence on the capacitor banks voltage, i.e., the reference voltage on the capacitor banks is attained with a satisfactory convergence. The wind perturbations are not a cause of significant influence on the capacitor banks voltage, i.e., the voltage on the capacitor banks is almost immune to the perturbations as an implication of what is seen on the behavior of the electric torque.

The DC currents for the submarine cable for one-mass (blue), two-mass (green) and three-mass (red), without and with wind perturbations are shown in Fig. 15.

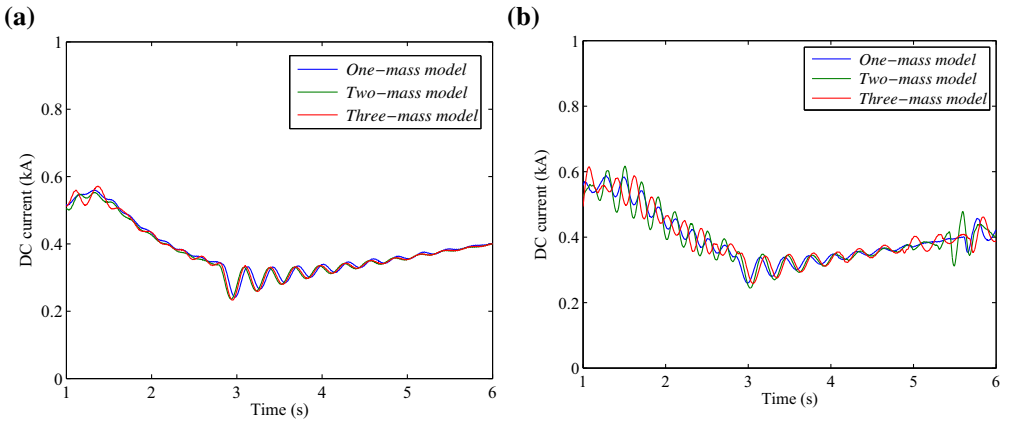

Fig. 15. One, two and three-mass model: DC current for the submarine cable. (a) Wind without perturbations; (b) wind with perturbations.

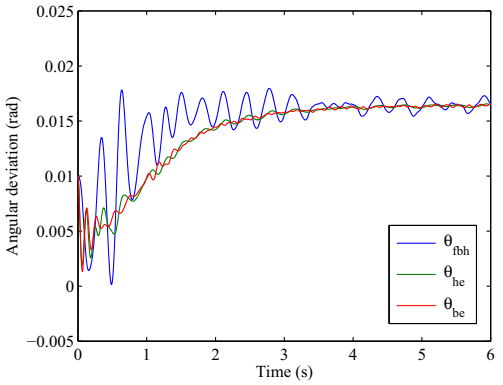

Fig. 16. Wind with perturbations, two and three-mass model: angular deviation.

For a wind without perturbations Fig. 15 shows that the DC current for the submarine cable presents an oscillatory behavior, with a more intense behavior for the three-mass model as expected due to the relevance of the added dynamics. For a wind with perturbations the DC currents have added small oscillations in comparison with the wind without perturbations.

The angular deviation of the flexible blade (blue), θ_{fbh}, the angular deviation of the rigid part of the blades plus hub (green), θ_{he}, for the three-mass model and the angular deviation of the generator (red), θ_{be}, for the two-mass model are shown in Fig. 16.

Fig. 16 shows an acceptable mechanical stress in the rotor in what regards the torsional effect, but the oscillations are better revealed with the three-mass modeling.

The average THD of the current injected in the electric grid for one-mass, two-mass and three-mass models are shown in Table 3.

Table 3 shows that with the TLC, the THD of the output current is lower than the 5% limit imposed by IEEE-519 standard [38], for the three mass models. The three-mass model shows more sensitive due to the system dynamics over the one-mass and the two-mass models in what regards THD values. The comparison of results for the wind with or without perturbations is primarily asserted with the three-mass model to conclude about the interested in having a more sensitivity modeling.

The three-mass model results for the submarine cable DC current harmonic behavior without perturbations (blue) or with perturbations (green) are shown in Fig. 17.

Table 3
THD of the current injected into the electric grid.

Output current	THD (%)		
	One-mass	Two-mass	Three-mass
Without perturbations	2.22	2.43	2.74
With perturbations	3.01	3.61	3.97

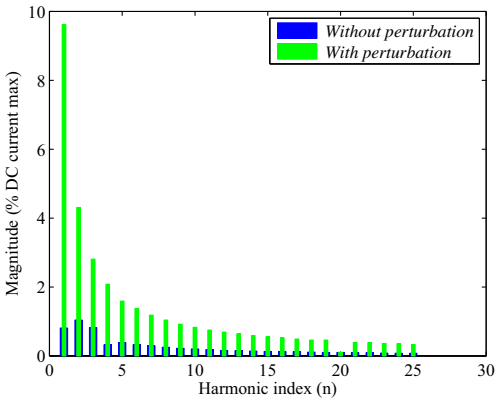

Fig. 17. Wind with or without perturbations, three-mass model: DC current harmonic index for the submarine cable.

Fig. 17 shows that the wind with perturbations introduces a harmonic behavior with larger component amplitudes while for the wind without perturbations components are almost negligible and is associated with the marine wave action.

7. Conclusions

A model for an OWTS is presented in order to reveal the interest in considering more than one discrete mass modeling for the drive train, taking into consideration the dynamics associated with the action excited by the wind and the marine waves on the physical structure. A TLC topology is simulated to connect the offshore turbine through a DC cable to the electrical grid. The simulations are carried out for one, two and three-mass drive train modeling to conclude on the total harmonic distortion associated with the energy injected into the electric grid and make an evaluation of how the perturbations on the energy captured due to the wind and the marine waves are attenuated at the injection point. The total harmonic distortion obtained by the simulations is not in favor of a particularly modeling, but nevertheless the three-mass drive train modeling reveals a more accurate observation of the stress behavior in what regards the torques and the angular deviations subjected by the rotor. The simulations are in favor of the model for the OWTS, revealing an adequate performance of the system. Additionally, the case studies prove that offshore OWTS is able to operate with adequacy enactment to the action due to the wind and the marine waves on the physical structure.

Acknowledgment

This work is funded by Portuguese Funds through the Foundation for Science and Technology-FCT under the Project LAETA 2015-2020, reference UID/EMS/50022/2013.

References

[1] J. Dashwood, The Outlook for Energy: a View to 2040, CEDA – Committee for Economic Development of Australia, Melbourn, 2012, pp. 45–52.

[2] M. Abdel-Akher, K. Mahmoud, Unbalanced distribution power-flow model and analysis of wind turbine generating systems, Eur. Trans. Electr. Power 23 (2013) 689–700.
[3] M. Tao, Y. Hongxing, L. Lin, A feasibility study of a stand-alone hybrid solar–wind–battery system for a remote island, Appl. Energy 121 (2014) 149–158.
[4] R. Melicio, V.M.F. Mendes, J.P.S. Catalão, Modeling and simulation of wind energy systems with matrix and multilevel power converters, IEEE Lat. Am. Trans. 7 (1) (2009) 78–84.
[5] P. Del Rio, M.A. Tarancón, Analysing the determinants of on-shore wind capacity additions in the EU: an econometric study, Appl. Energy 95 (2012) 12–21.
[6] B. Ge, F.Z. Peng, Current balancer-based grid-connected parallel inverters for high power wind-power system, Int. Trans. Electr. Energy Syst. 24 (2014) 108–124.
[7] X. Wang, W. Teng, L. Ning, Y. Meng, Z. Xu, Feasibility of integrating large wind farm via fractional frequency transmission system a case study, Int. Trans. Electr. Energy Syst. 24 (2014) 64–74.
[8] J. Wu, Z.X. Wang, G.Q. Wang, The key technologies and development of offshore wind farm in China, Renew. Sustainable Energy Rev. 34 (2014) 453–462.
[9] M. Guan, Z. Xu, A novel concept of offshore wind-power collection and transmission system based on cascaded converter topology, Int. Trans. Electr. Energy Syst. 24 (2014) 363–377.
[10] M. Esteban, D. Leary, Current developments and future prospects of offshore wind and ocean energy, Appl. Energy 90 (2012) 128–136.
[11] B. Lange, S. Larsen, J. Højstrup, R. Barthelmie, Importance of thermal effects and sea surface roughness for offshore wind resource assessment, J. Wind Eng. Ind. Aerodyn. 92 (11) (2004) 959–988.
[12] N. Luo, C.L. Bottasso, H.R. Karimi, M. Zapateiro, Semiactive control for floating offshore wind turbines subject to aero-hydro dynamic loads, in: Proceedings of the International Conference on Renewable Energies and Power Quality – ICREPQ'11, Las Palmas de Gran Canaria, 2011, pp. 1–6.
[13] M. Tudorov, G. Vukov, Parametric torsional vibrations of a drive train in horizontal axis wind turbine, in: Proceedings of the 1ère Conférence Franco-Syrienne sur les Energies Renouvelables, Damascus, 2010, pp. 1–17.
[14] Z.X. Xing, L.Z. Liang, H.Y. Guo, X.D. Wang, Damping control study of the drive train of DFIG wind turbine, in: Proceedings of the International Conference on Energy and Environment Technology, Taj Chandigarh, 2009, pp. 576–579.
[15] M. Seixas, R. Melicio, V.M.F. Mendes, Fifth harmonic and sag impact on PMSG wind turbines with a balancing new strategy for capacitor voltages, Energy Convers. Manage. 74 (2014) 721–730.
[16] E. Pican, E. Omerdic, D. Toal, M. Leahy, Direct interconnection of offshore electricity generators, Energy 36 (3) (2011) 1543–1553.
[17] M. Dicorato, G. Forte, M. Trovato, Wind farm stability analysis in the presence of variable-speed generators, Energy 39 (1) (2012) 40–47.
[18] L. Whei-Min, H. Chih-Ming, Intelligent approach to maximum power point tracking control strategy for variable-speed wind turbine generation system, Energy 35 (6) (2010) 2440–2447.
[19] N.B. Negra, J. Todorovic, T. Ackermann, Loss evaluation of HVAC and HVDC transmission solutions for large offshore wind farms, Electric Power Syst. Res. 76 (11) (2006) 916–927.
[20] E. Balogh, Deepwater Offshore Wind Power Generation Using Oil and Gas Platform Technology. <http://www.renewableenergyworld.com/rea/news/article/2008/12/deepwater-offshore-wind-power-generation-using-oil-and-gas-platform-technology-54314;2008> [Online; accessed 18-December-2014].
[21] S. Ambühl, M. Sterndorff, J.D. Sørensen, Extrapolation of extreme response for different mooring line systems of floating wave energy converters, Int. J. Mar. Energy 7 (2014) 1–19.
[22] V. Akhmatov, H. Knudsen, A.H. Nielsen, Advanced simulation of windmills in the electric power supply, Int. J. Electr. Power Energy Syst. 22 (6) (2000) 421–434.
[23] J.G. Slootweg, H. Polinder, W.L. Kling, Representing wind turbine electrical generating systems in fundamental frequency simulations, IEEE Trans. Power Syst. 18 (4) (2003) 516–524.
[24] F.N. Eikeland, Compensation of wave-induced motion for marine crane operations (Msc. Thesis), Norwegian University of Science, 2008, pp. 16–26.
[25] M. Seixas, R. Melício, V.M.F. Mendes, Simulation of offshore wind turbine link to the electric grid through a four-level converter, in: L.M. Camarinha-Matos, N.S. Barrento, R. Mendonça (Eds.), 5th DoCEIS 2014, Technological Innovation Collective Awareness Systems, Springer, Heidelberg, 2014, pp. 324–331.
[26] J. Holierhoek, Investigation into the possibility of flap-lag-stall flutter, in: Proceedings of the 45th AIAA Aerospace Sciences Meeting and Exhibit, Reno, 2007, pp. 1–12.
[27] P.K. Chaviaropoulos, Flap/lead-lag aeroelastic stability of wind turbine blade sections, Wind Energy 2 (1999) 99–112.
[28] G. Ramtharan, N. Jenkins, Influence of rotor structural dynamics representations on the electrical transient performance of DFIG wind turbines, Wind Energy 10 (4) (2007) 293–301.
[29] J.F. Manwell, J.G. McGowan, A.L. Rogers, Wind Energy Explained: Theory, Design and Application, second ed., Wiley, West Sussex, 2009. pp. 83–105.
[30] C.M. Ong, Dynamic Simulation of Electric Machinery: Using Matlab/Simulink, Prentice-Hall, New Jersey, 1998, pp. 259–350.
[31] T. Senjyu, S. Tamaki, N. Urasaki, K. Uezato, Wind velocity and position sensorless operation for PMSG wind generator, in: Proceedings of the 5th International Conference on Power Electronics and Drive Systems, Singapore, 2003, pp. 787–792.
[32] M. Seixas, R. Melicio, V.M.F. Mendes, H.M.I. Pousinho, Simulation of offshore wind system with two-level converters: HVDC power transmission, in: Proceedings of the 16th International Power Electronics and Motion Control Conference and Exposition, Antalya, Turkey, 2014, pp. 1384–1389.
[33] R. Melício, V.M.F. Mendes, Simulation of power converters for wind energy systems, Inf. Tecnol. 18 (4) (2007) 25–34.
[34] A. Biswas, S. Das, A. Abraham, S. Dasgupta, Design of fractional-order (PID mu)-D-lambda controllers with an improved differential evolution, Eng. Appl. Artif. Intell. 22 (2) (2009) 343–350.
[35] A.J. Calderón, B.M. Vinagre, V. Feliu, Fractional order control strategies for power electronic buck converters, Signal Process 86 (10) (2006) 2803–2819.

[36] G. Maione, P. Lino, New tuning rules for fractional PI-alfa controllers, Nonlinear Dyn. 49 (1–2) (2007) 251–257.
[37] S.M. Muyeen, A. Al-Durra, J. Tamura, Variable speed wind turbine generator system with current controlled voltage source inverter, Energy Convers. Manage. 52 (7) (2011) 2688–2694.
[38] IEEE Guide for Harmonic Control and Reactive Compensation of Static Power Converters, IEEE Standard 519-1992, 1992.